# Compact substrate-removed thin-film lithium niobate electro-optic modulator featuring polarization-insensitive operation

Ying Pan,[1] Mingbo He,[1] Mengyue Xu,[1] Zhongjin Lin,[2,3] Yanmei Lin,[1] Wei Ke,[1] Jie Liu,[1] Zhenrui Lin,[1] Yuntao Zhu,[1] Shenqian Gao,[1] Hao Li,[1] Xiaoyue Liu,[1] Chuan Liu,[1] Siyuan Yu,[1] and Xinlun Cai[1,4]

[1] *State Key Laboratory of Optoelectronic Materials and Technologies and School of Electronics and Information Technology, Sun Yat-sen University, Guangzhou, China*
[2] *Department of Electrical and Computer Engineering, The University of British Columbia, Vancouver, BC V6 T 1Z4, Canada*
[3] *e-mail: zlin23@ece.ubc.ca*
[4] *e-mail: caixlun5@mail.sysu.edu.cn*

**A compact polarization-insensitive electro-optic (EO) modulator, which allows the laser and modulator to be located at different locations while using a standard single-mode fiber to interconnect them, is highly desirable for 5G or future 6G wireless networks. Herein, we propose a modulator based on substrate-removed thin-film lithium niobate. The proposed device exhibits a polarization-dependent loss of 0.35 dB and on-chip loss of approximately 2 dB. The polarization insensitivity of the proposed device was experimentally demonstrated using a four-level pulse-amplitude modulation format at 50 Gbaud (100 Gb/ s).** © 2022 Optica Publishing Group

Electro-optic (EO) modulators are critical components of various optical links, including optical telecommunications, data centers, and wireless communication systems. For 5G and future 6G wireless communication systems, a compact EO modulator featuring polarization-independent operation is highly desirable. As shown in Fig. 1(a), this modulator allows a remote laser source to be employed through a standard single-mode fiber without the assistance of a polarization controller [1,2]. Thus, the laser source can be placed in a thermally controlled environment to maintain a high performance. Laser sources, co-packaged or integrated with EO modulators, are normally required to be operated within a temperature range of 0 to 70°C to avoid significant degradation of their performance and reliability. This temperature range can be easily achieved in thermally controlled environments such as optical transceivers in data centers. However, for 5G or future 6G wireless communication systems, a large number of antenna elements and the associated digital application-specific integrated circuits (ASICs) need to be placed close to EO modulators, leading to a high-temperature environment (>100°C) for co-packaged or integrated laser sources [1,3,4]. Therefore, connecting remote laser sources with polarization-insensitive EO modulators through a standard

single-mode fiber would be a cost-effective way to address this issue.

Many polarization-insensitive EO modulators have been proposed based on various material platforms such as silicon-on-insulator [5], polymers [6], graphene-assisted or indium tin oxide-assisted silicon-on-insulator [7–9], gallium, and zinc-and-nickel in diffused lithium niobate (LN) [10]. Few of them have been experimentally demonstrated in high-speed transmission.

Recently, the thin-film LN (TFLN) platform has emerged as a promising platform for compact and high-performance EO modulators because of its advantages of low drive voltage, low optical loss, and ultrafast modulation [11,12]. Moreover, the LN material exhibits very good temperature stability, making it attractive for use in future wireless communication systems.

Here, for the first time, to the best of our knowledge, a polarization-insensitive EO modulator based on substrate-removed TFLNs is presented. Polarization independence is achieved using a polarization-diversity scheme [13]. A polarization splitter-rotator (PSR) is used to map two orthogonal linearly polarized components of incoming light into two separate arms with a fundamental transverse electric (TE) mode. The two arms are then modulated by two Mach–Zehnder modulators (MZMs) that have the same modulation efficiency and share the same traveling-wave electrodes. On the output side, another PSR is used to rotate the polarization state in one of the arms and recombine the two arms. Through this scheme, the proposed device can realize polarization-insensitive operation. The proposed device can achieve a polarization-dependent loss of 0.35 dB, and on-chip loss of 2 dB. Additionally, we experimentally demonstrate polarization-insensitive operation of the proposed device using a four-level pulse-amplitude modulation (PAM-4) format at 50 Gbaud.

A schematic of the proposed device is shown in Fig. 1(b). The proposed device included two PSRs and two MZMs. The PSR was used to map the two orthogonal linearly polarized components of incoming light into two fundamental TE-guided modes. Thus, single polarization could be achieved on the chip. The
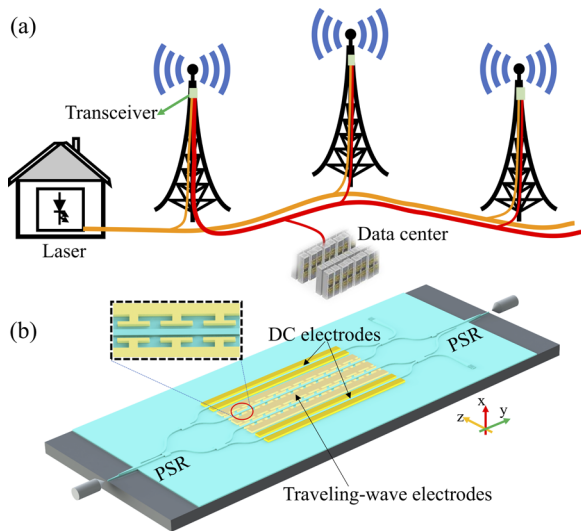
**Fig. 1.** (a) Concept of a 5G or future 6G wireless network system using the polarization-insensitive electric-optic modulators. (b) A schematic of the proposed polarization-insensitive electric-optic modulator. PSR, polarization splitter-rotator; DC, direct current.

two polarization rotations were performed on opposite arms to achieve overall symmetry and compensate for the polarization-dependent loss caused by the PSR [13]. The principles and performance of the proposed PSR are discussed below.

The two arms of light were modulated by two MZMs, but the two MZMs shared the same ground-signal-ground (GSG) traveling-wave electrodes. Each MZM had one arm that lies in the gap between the ground and signal electrodes. This architecture allowed the two MZMs to be driven simultaneously using only one traveling-wave electrode. The traveling-wave electrodes were capacity-loaded traveling-wave electrodes, which allowed a low drive voltage as well as a large EO bandwidth [Fig. 1 (b)] [14]. Compared with the general electrodes, the capacity-loaded traveling-wave electrodes can break the trade-off between the microwave loss and the drive voltage [15]. Here, we used a substrate removal technique to partially remove the Si substrate underneath the traveling-wave electrode, which further reduced microwave loss [16]. Here, the direct current (DC) bias point of the MZM was controlled by the EO effect. The conventional coplanar strip line configuration was used to build the DC electrodes.

The proposed device was fabricated on an X-cut TFLN wafer (NanoLN). The wafer consisted of a 360-nm TFLN layer on a 500-µm-thick silicon handle with a 4.7-µm buried oxide layer. The rib waveguide with an etch depth of 180 nm was used in this work. First, LN waveguides were patterned by electron beam lithography (EBL) and formed by argon plasma etching (APE). The device was then coated with a layer of 1-µm silica. Next, 900-nm-thick gold traveling-wave electrodes and a layer of 5-nm-thick Ti were patterned by EBL and deposited by electron beam evaporation (EBE). Subsequently, the Si substrate underneath the traveling-wave electrode was removed by etching the adjacent LN, SiO$_2$ layer, and Si substrate. Finally, edge couplers were formed by polishing (Logitech PM6) [17,18].

Figure 2(a) shows a micrograph of the fabricated device. Figures 2(b) and 2(c) present pseudo-color scanning electron microscopy (SEM) images of the modulation region. The LN full etch areas include the edge coupler section, and the LN window opened for substrate removal. The total length of the traveling-wave electrodes was 20 mm, and the electrode gap was 3.8 µm. The size and period of the microstructure of the traveling-wave electrodes were 45 µm × 1 µm and 50 µm, respectively. The cross-sectional view of the fabricated device, shown in Fig. 2(d), indicated that the substrate was successfully removed.

The proposed PSR was based on a two-stage adiabatic mode evolution process, including a mode evolution taper and asymmetrical directional coupler, as shown in the inset of Fig. 3. The mode evolution taper was used to rotate the polarization state from the fundamental transverse magnetic (TM) mode to the TE$_1$ mode. An asymmetrical directional coupler was used to split the
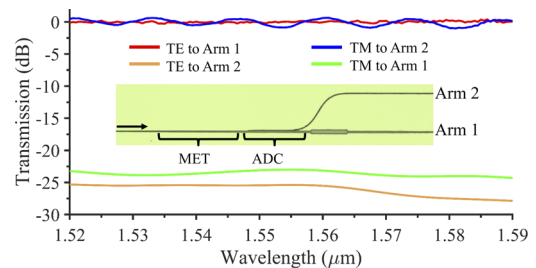


**Fig. 3.** Transmission of the fabricated polarization splitter-rotator (PSR) when injecting TE (lighter from top two and first from bottom lines) and TM (darker from top two and second from bottom lines) polarization. Inset shows the micrograph of the fabricated PSR. MET, mode evolution taper; ADC, asymmetrical directional coupler.
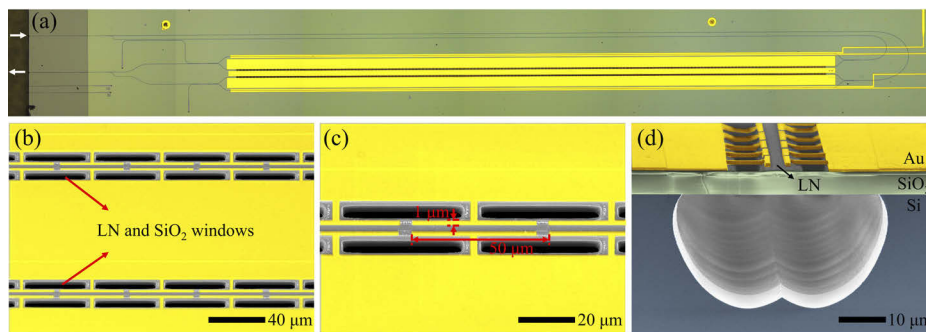


**Fig. 2.** (a) Micrograph of the fabricated device. (b) and (c) Pseudo-color scanning electron microscopy (SEM) images of the top view of the modulation region. The LN and SiO$_2$ windows labeled in (b) are opened for substrate removal. (d) Pseudo-color SEM image of the cross-sectional view of the fabricated device.
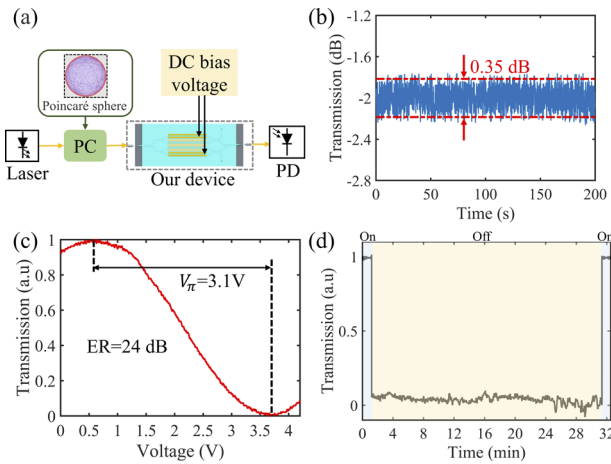
**Fig. 4.** (a) Schematic of the experimental setup used for characterizing the on-chip insertion loss and polarization-dependent loss of the fabricated device. PC, commercial polarization controller; PD, photodetector. (b) On-chip transmission of the fabricated device as a function of time when the input polarization states vary with a scrambling rate of 100 rad/s. (c) Normalized optical transmission of the fabricated device as a function of the applied voltage. (d) On and off states of the MZM controlled by the DC electrodes based on the EO effect.
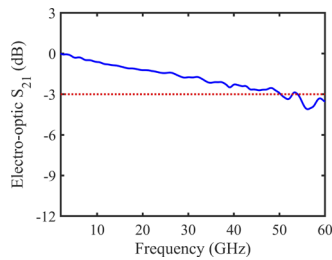


**Fig. 5.** Small-signal electro-optic response of the fabricated device with a 20-mm length of the traveling wave electrode.

$TE_0$ and $TE_1$ modes and convert the $TE_1$ mode to the $TE_0$ mode. More details regarding the design of the PSR can be found in our previous study [19]. The fabricated PSR featured a polarization crosstalk of $\sim 23$ dB, an operation bandwidth of $> 70$ nm, and an on-chip insertion loss of $<0.12$ dB (see Fig. 3). The on-chip losses were separated from the fiber-to-chip coupling losses by performing additional waveguide coupling tests. The fiber-to-chip coupling losses of TE and TM modes were near 2 dB. The polarization-dependent loss of the fabricated edge coupler was near 0.3 dB.

The on-chip insertion loss and polarization-dependent loss of the fabricated device were characterized using a commercial polarization controller (PSY 201, General Photonics) with a polarization scrambling of 100 rad/s [Fig. 4(a)]. Within 200 s, the input polarization states completely covered the surface of the Poincaré sphere. The corresponding on-chip transmissions of the fabricated device are shown in Fig. 4(b). The results revealed that the fabricated device can achieve an on-chip insertion loss of 2 dB and a polarization-dependent loss of 0.35 dB.

The two MZMs had the same half-wave voltages ($V_\pi$) of 3.1 V with the modulation length of 20 mm and achieved an extinction ratio of 24 dB [Fig. 4(c)]. The modulation efficiency ($V_\pi L$) can be improved if the differential-drive traveling-wave electrode is used in the future. Although the proposed device had a low modulation efficiency, its $V_\pi$ (i.e., drive voltage) was still lower than that of many optical modulators which have similar EO bandwidth. We will show the EO bandwidth of our device in the following. Figure 4(d) presents the on and off states of the MZM controlled by the DC electrodes, exhibiting a high stability of the DC bias point controlled by EO effect. From 1 min to 31 min in Fig. 4(d), the voltage applied to the DC electrodes was fixed. Using the EO effect to control the modulation bias point can not only decrease the power consumption but also significantly improve the temperature stability of the proposed device.

A vector network analyzer (Agilent N5227A) with a bandwidth of up to 67 GHz was used to characterize the electro-optic response of the fabricated modulator at a telecom wavelength of 1550 nm. The substrate removal not only can improve the microwave loss but also can finely tune the microwave index
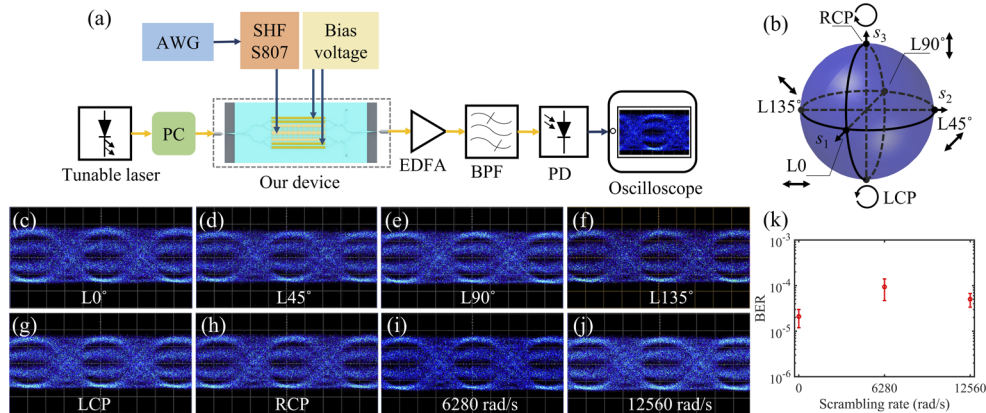


**Fig. 6.** (a) Experimental setup for four-level pulse-amplitude modulation (PAM-4) transmission. AWG, arbitrary waveform generator; PC, commercial polarization controller; EDFA, Erbium-doped fiber amplifier; SHF, super high frequency amplifier; BPF, Berkeley packet filter; PD, photodetector. (b) Six input polarization states of linear at 0° (L0°), linear at 45° (L45°), linear at 90° (L90°), linear at 135° (L135°), left-handed circular polarization (LCP), and right-handed circular polarization (RCP) shown on the Poincaré sphere. (c)–(h) Measured eye diagrams when the input polarization states are set at L0°, L45°, L90°, L135°, LCP, and RCP, respectively. (i) and (j) Measured eye diagrams when the input SOPs are scrambled at the rates of 6.28 Krad/s and 12.56 Krad/s, respectively. (k) Bit error rate (BER) of our device when the input SOPs were scrambled at different speed. In all cases, our device was driven by the AWG with a PAM-4 format at a symbol rate of 50 Gbaud (100 Gb/s).

[16]. Figure 5 indicates that the fabricated device achieved a 3-dB EO bandwidth of 50 GHz with a 20-mm length of the traveling wave electrode.

Next, we evaluated the performance of the fabricated device for high-speed digital data transmission. Figure 6(a) shows a schematic of the experimental setup. A commercial polarization controller (PSY 201, General Photonics) was used to manage the state of polarization (SOP) of incoming light. To characterize the performance of high-speed modulation, an arbitrary waveform generator (AWG, Micram) was used to drive the traveling-wave electrodes, and the output optical signal was detected by a high-speed detector (Finisar, XPDV3120R) after being amplified by an erbium-doped fiber amplifier (EDFA) and passed through a bandpass filter. A microwave oscilloscope (Agilent DCA-X86100D) was used to characterize the eye diagram of the output signal. In the following experiments, our device was driven by the AWG with the PAM-4 format at 50 Gbaud.

To characterize the performance of the fabricated device in response to different input polarization states, four linear polarization states at 0° (L0°), 45° (L45°), 90° (L90°), 135° (L135°), and two circular left-handed polarization (LCP) and right-handed polarization (RCP) states were injected into the fabricated device. The six polarization states visualized on the Poincaré sphere are shown in Fig. 6(b). Figures 6(c)–6(h) present the measured eye diagrams of the fabricated device in response to the six polarization states. Opening eye diagrams were observed in all cases, indicating that the proposed device exhibits strong polarization-insensitive operation. To further verify this insensitivity, the input SOPs were scrambled at rates of 6.28 Krad/s and 12.56 Krad/s. The corresponding eye pattern results are presented in Figs. 6(i) and 6(j). We observed that the proposed device still exhibited an open eye pattern. Figure 6(k) indicates that the bit error rate (BER) was always maintained at lower than the forward error correction (FEC) threshold in all cases shown in Figs. 6(c)–6(j).

In conclusion, based on the TFLN platform, we propose and experimentally demonstrate a polarization-insensitive modulator that can be directly connected to a remote laser source through a standard single-mode fiber. The proposed device exhibits a polarization-dependent loss of 0.35 dB and on-chip loss of approximately 2 dB. By using the capacity-loaded traveling-wave electrodes and substrate removal technique, our device can achieve a 3-dB EO bandwidth of 50 GHz with a 20-mm length of the traveling electrode. The proposed device has huge potential for 5G or future 6G wireless networks and provides a cost-effective transceiver that can be used in extreme environments.

## REFERENCES

1. B. Buscaino, E. Chen, J. W. Stewart, T. Pham, and J. M. Kahn, J. Lightwave Technol. **39**, 1984 (2021).
2. A. Bigongiari, L. Giorgi, G. De Angelis, A. Serrano Rodrigo, M. Chiesa, D. Rotta, S. Tirelli, L. Tallone, M. Romagnoli, and F. Testa, J. Lightwave Technol. **40**, 519 (2021).
3. F. Testa, M. Wade, M. Lostedt, F. Cavaliere, M. Romagnoli, and V. Stojanovic, J. Lightwave Technol. **40**, 393 (2021).
4. P. Iovanna, A. Bigongiari, F. Cavaliere, A. Bianchi, F. Testa, S. Marconi, M. Romagnoli, V. Sorianello, A. Sgambelluri, F. Denise-Le Coarer, L. Milord, M. Peyrou, and S. Menezo, J. Lightwave Technol. **40**, 527 (2021).
5. X. Guan, M. Lyu, W. Shi, and L. Rusch, J. Lightwave Technol. **40**, 744 (2022).
6. A. Donval, E. Toussaere, R. Hierle, and J. Zyss, Synth. Met. **115**, 21 (2000).
7. X. Zou, Y. Zhang, Z. Li, Y. Yang, S. Zhang, Z. Zhang, Y. Zhang, and Y. Liu, Appl. Sci. **9**, 429 (2019).
8. Y. Xu, F. Li, Z. Kang, D. Huang, X. Zhang, H. Y. Tam, and P. K. A. Wai, Nanomaterials **9**, 157 (2019).
9. X. Hu and J. Wang, Nanophotonics **7**, 651 (2018).
10. A. Kaplan and S. Ruschin, IEEE J. Sel. Top. Quantum Electron. **6**, 83 (2000).
11. M. Xu, M. He, H. Zhang, J. Jian, Y. Pan, X. Liu, L. Chen, X. Meng, H. Chen, Z. Li, X. Xiao, S. Yu, S. Yu, and X. Cai, Nat. Commun. **11**, 3911 (2020).
12. C. Wang, M. Zhang, X. Chen, M. Bertrand, A. Shams-Ansari, S. Chandrasekhar, P. Winzer, and M. Loncar, Nature **562**, 101 (2018).
13. T. Barwicz, M. R. Watts, M. A. Popović, P. T. Rakich, L. Socci, F. X. Kärtner, E. P. Ippen, and H. I. Smith, Nat. Photonics **1**, 57 (2007).
14. P. Kharel, C. Reimer, K. Luke, L. He, and M. Zhang, Optica **8**, 357 (2021).
15. X. Liu, B. Xiong, C. Sun, Z. Hao, L. Wang, J. Wang, Y. Han, H. Li, J. Yu, and Y. Luo, in *Asia Communications and Photonics Conference* (Optical Society of America, 2020), paper M4A.144.
16. M. Li, L. Wang, X. Li, X. Xiao, and S. Yu, Photonics Res. **6**, 109 (2018).
17. X. Liu, P. Ying, X. Zhong, J. Xu, Y. Han, S. Yu, and X. Cai, Opt. Lett. **45**, 6318 (2020).
18. P. Ying, H. Tan, J. Zhang, M. He, M. Xu, X. Liu, R. Ge, Y. Zhu, C. Liu, and X. Cai, Opt. Lett. **46**, 1478 (2021).
19. Z. Lin, Y. Lin, H. Li, M. Xu, M. He, W. Ke, Y. Han, Z. Li, D. Wang, X. S. Yao, S. Yu, and X. Cai, "High performance polarization management devices based on thin-film lithium niobate," arXiv:2110.04508 (2021).